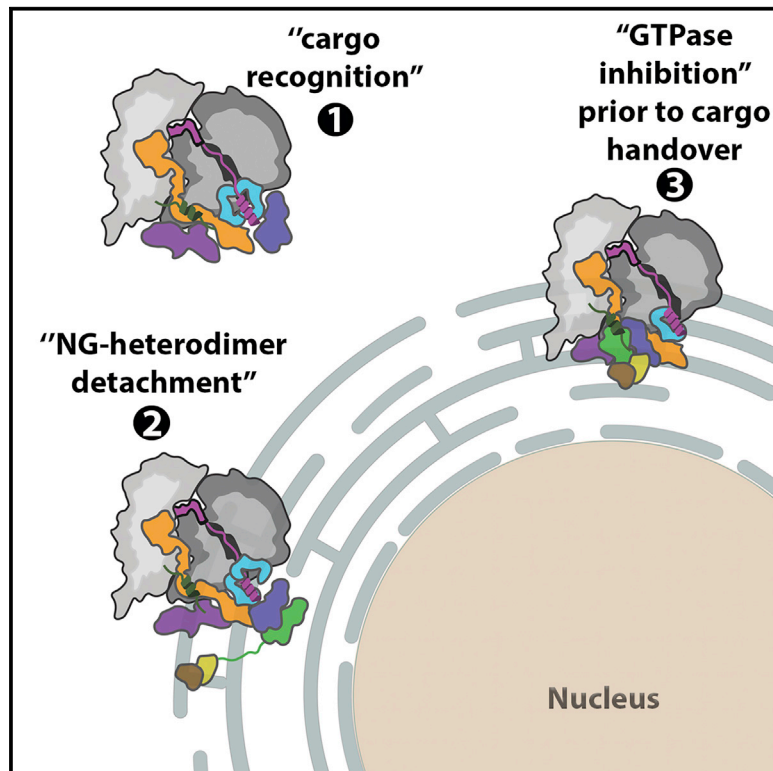


# Molecular mechanism of cargo recognition and handover by the mammalian signal recognition particle

## Graphical abstract



## Authors

Ahmad Jomaa, Simon Eitzinger, Zikun Zhu, Sowmya Chandrasekar, Kan Kobayashi, Shu-ou Shan, Nenad Ban

## Correspondence

ahmad.jomaa@mol.biol.ethz.ch (A.J.), sshan@caltech.edu (S.-o.S.), ban@mol.biol.ethz.ch (N.B.)

## In brief

Jomaa et al. present cryo-EM structures of mammalian SRP, SRP receptor, and the translating ribosome. The structures reveal the role of eukaryotic-specific features involved in regulating early and late stages of co-translational protein targeting to the endoplasmic reticulum and suggest a model for cargo recognition and handover.

## Highlights

- Cryo-EM reveals the molecular features of the mammalian SRP targeting complexes
- The fold of the eukaryotic SRP54 M domain and signal sequence binding is revealed
- SRP·SR complex reveals eukaryotic-specific SRP contacts at the distal site
- Regulation of the SRP·SR GTPase occurs through conserved protein and RNA contacts



## Article

# Molecular mechanism of cargo recognition and handover by the mammalian signal recognition particle

Ahmad Jomaa,<sup>1,\*</sup> Simon Eitzinger,<sup>1,3</sup> Zikun Zhu,<sup>2</sup> Sowmya Chandrasekar,<sup>2</sup> Kan Kobayashi,<sup>1</sup> Shu-ou Shan,<sup>2,\*</sup> and Nenad Ban<sup>1,4,\*</sup>

<sup>1</sup>Department of Biology, Institute of Molecular Biology and Biophysics, ETH Zurich, 8093 Zurich, Switzerland

<sup>2</sup>Division of Chemistry and Chemical Engineering, California Institute of Technology, Pasadena, CA, USA

<sup>3</sup>Present address: Harvard Medical School, Boston, MA 02115, USA

<sup>4</sup>Lead contact

\*Correspondence: [ahmad.jomaa@mol.biol.ethz.ch](mailto:ahmad.jomaa@mol.biol.ethz.ch) (A.J.), [sshan@caltech.edu](mailto:sshan@caltech.edu) (S.-o.S.), [ban@mol.biol.ethz.ch](mailto:ban@mol.biol.ethz.ch) (N.B.)  
<https://doi.org/10.1016/j.celrep.2021.109350>

## SUMMARY

Co-translational protein targeting to membranes by the signal recognition particle (SRP) is a universally conserved pathway from bacteria to humans. In mammals, SRP and its receptor (SR) have many additional RNA features and protein components compared to the bacterial system, which were recently shown to play regulatory roles. Due to its complexity, the mammalian SRP targeting process is mechanistically not well understood. In particular, it is not clear how SRP recognizes translating ribosomes with exposed signal sequences and how the GTPase activity of SRP and SR is regulated. Here, we present electron cryo-microscopy structures of SRP and SRP·SR in complex with the translating ribosome. The structures reveal the specific molecular interactions between SRP and the emerging signal sequence and the elements that regulate GTPase activity of SRP·SR. Our results suggest the molecular mechanism of how eukaryote-specific elements regulate the early and late stages of SRP-dependent protein targeting.

## INTRODUCTION

Membrane proteins make up almost 30% of the cell proteome and are targeted to the membrane while being synthesized on the ribosome (Akopian et al., 2013). The co-translational targeting of these proteins to the endoplasmic reticulum (ER) or to the bacterial cell membrane is carried out by the universally conserved signal recognition particle (SRP) and its receptor (SR) (Akopian et al., 2013; Gilmore et al., 1982b; Nyathi et al., 2013). In bacteria, the best-studied SRP is from *Escherichia coli* and is composed of one RNA molecule (4.5S) and one protein, Ffh, also known as homolog of eukaryotic SRP54; whereas SR is composed of one protein, FtsY (Zhang and Shan, 2014). Both Ffh and FtsY contain homologous NG domains with guanine triphosphatase (GTPase) modules that assemble into the NG heterodimer in the presence of GTP and disassemble upon GTP hydrolysis. In addition to the NG domain, Ffh contains a methionine-rich domain (M domain) that recognizes and binds the emerging N-terminal signal sequence or a trans-membrane domain (TMD) of the nascent polypeptide chain on the translating ribosome, referred to as ribosome nascent chain complex (RNC). In addition to the NG domain, FtsY contains an N-terminal A domain with two amphipathic regions that bind the cell membrane and the SecYEG translocation machinery in bacteria (Draycheva et al., 2016; Hwang Fu et al., 2017; Park and Rapoport, 2012).

In eukaryotes, SRP and SR have undergone an extensive expansion at both the RNA level and the protein level. The mammalian SRP contains a larger RNA (7SL) and 6 proteins (SRP19, SRP9/SRP14 heterodimer, SRP54, SRP68, and SRP72) (Gilmore et al., 1982a, 1982b). Mammalian SR is an  $\alpha/\beta$  heterodimer. SR $\alpha$  contains an N-terminal X domain and a C-terminal NG domain separated by a 170-amino acid unstructured linker that is rich in positive residues. SR $\beta$  is a membrane-anchored protein containing an N-terminal TMD and a G domain that binds GTP to form a heterodimer with the X domain of SR $\alpha$  (SRX/ $\beta$  heterodimer) (Miller et al., 1995; Tajima et al., 1986; Young et al., 1995).

A long-standing question in the eukaryotic SRP targeting pathway is how early and late events of co-translational protein targeting are modulated to allow the transition from cargo recognition to cargo handover mode—in particular, how the nascent chain and the emerging sequence are recognized, how the GTPase activity of SRP54 and SR is regulated at the SRP RNA distal site, and finally what events lead to cargo handover to the Sec translocon. Previous studies provided functional and structural insights into the SRP, SRP-SR, or Sec61 interactions with the ribosome exit tunnel (Becker et al., 2017; Grotwinkel et al., 2014; Halic et al., 2006a; Hwang Fu et al., 2019; Jadhav et al., 2015a; Jiang et al., 2008; Kobayashi et al., 2018; Lee et al., 2018; Mandon et al., 2003; Pfeffer et al., 2017; Schwartz and Blobel, 2003; Voorhees and Hegde, 2015, 2016; Voorhees et al., 2014; Wild et al., 2019). The functional



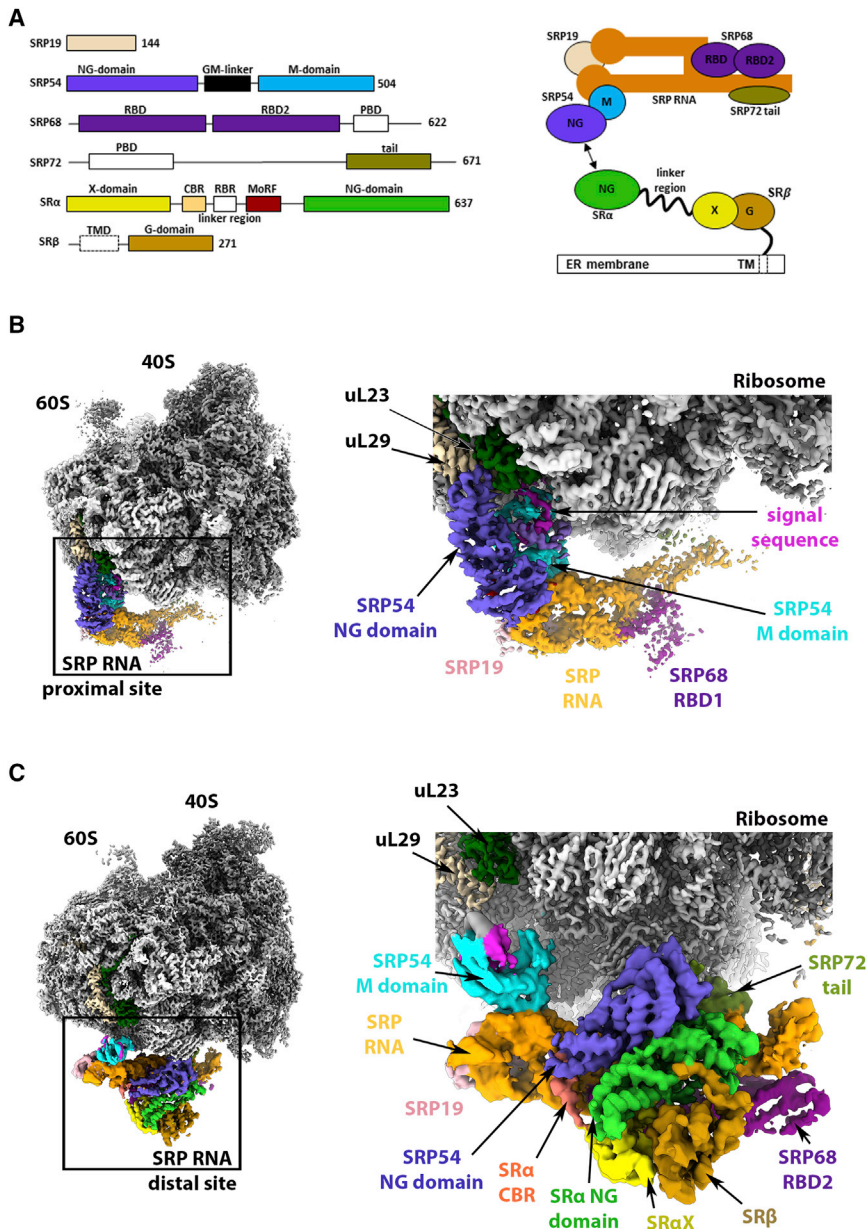


**Figure 1. Cryo-EM maps of the mammalian SRP targeting complexes**

(A) Left panel, domain architecture of the SRP proteins SRP19 (pink), SRP54, SRP68 (RNA binding domain [RBD] purple), SRP72 (protein binding domain [PBD] is white and the C-terminal tail is olive), and the 2 proteins of the SRP receptor, SR $\alpha$  and SR $\beta$ . SRP54 NG and M domains (slate blue and cyan), and the GM-linker (medium blue) are indicated. SRX, NG, CBR (channel binding region), RBR (ribosome binding region), and MoRF (molecular recognition feature), are yellow, green, salmon, gray, and cherry red, respectively. The SR $\beta$  G domain is golden brown, and the membrane anchor TMD is white.

(B) Cryo-EM map of the mammalian SRP targeting complex with the translating mammalian ribosome. The large (60S) and small (40S) ribosomal subunits are light and dark gray, respectively. The cryo-EM density of the SRP complex on the ribosome is colored the same as in (A). The SRP-bound signal sequence and the emerging nascent chain is magenta. Ribosomal protein uL23 and uL29 are colored olive green and wheat, respectively.

(C) Composite cryo-EM map of the RNC·SRP·SR complex. The large (60S) and small (40S) ribosomal subunits are colored light and dark gray, respectively. The SRP and SR are colored the same as in (A). Ribosomal proteins uL23 and uL29 are olive green and wheat, respectively. See also [Figures S1](#) and [S3](#).

interpretations of the SRP and SR features on the ribosome, however, were limited to intermediate resolution (5–10 Å). Therefore, our mechanistic understanding of different stages of co-translational protein targeting to membranes in eukaryotes is incomplete. Furthermore, the involvement of eukaryotic-specific elements in modulating this highly conserved pathway underscores the divergence in SRP function during evolution and is of particular interest due to their role in cellular homeostasis and onset of human disease. For example, the C-terminal tail of SRP72 is selectively phosphorylated and further cleaved upon apoptosis ([Becker et al., 2017](#); [Utz et al., 1998](#)). Mutations in SRP54, SRP72, and SR $\alpha$  were also identified in patients with congenital neutropenia with Shwachman-Diamond-like features

and familial aplasia and myelodysplasia ([Bellanné-Chantelot et al., 2018](#); [D’Altri et al., 2019](#); [Kirwan et al., 2012](#); [Konantz et al., 2018](#)).

To reveal the molecular basis of the early stages of SRP-mediated protein targeting to ER, we determined two cryo-electron microscopy (cryo-EM) structures of a mammalian early SRP and late SRP·SR targeting complexes with the translating ribosome. The structures of the early SRP and late SRP·SR intermediates on the ribosome together define the molecular and structural mechanisms required for eukaryotic SRP cargo recognition in the vicinity of the ribosome tunnel region. Together with biochemical data, the structures also reveal the mechanism of GTPase regulation at the distal site of the SRP RNA that is critical for signal sequence handover to the translocon.

## RESULTS

### The cryo-EM structures of mammalian SRP and SRP·SR targeting complexes

The first of the two mammalian targeting complexes, an RNC·SRP complex with the SRP54 NG-domain at the proximal site of the SRP RNA along with the M-domain bound to the signal sequence, was resolved to 3.0 Å ([Figures 1](#), [S1](#), and [S2](#); [Table 1](#)).

**Table 1. Cryo-EM data collection, map refinement, model refinement, and validation statistics**

Structure	RNC·SRP	RNC·SRP·SR
EMDB accession, PDB code	EMD-12801, 7OBR	EMD-12799, 7OBQ/EMD-12800
<b>Data collection</b>		
Microscope	FEI Titan Krios	
Detector	Gatan K3	
Voltage (keV)	300	
Electron exposure (e <sup>-</sup> /Å <sup>2</sup> )	50	
Pixel size (Å)	1.07	
Magnification (preGif)	81,000×	
Defocus range (μm)	1.5–2.5	
Automation software	EPU/SerialEM	
<b>EM reconstruction</b>		
Final particles (no.)	43,135	155,989
Resolution (unmasked/masked) at FSC = 0.143 (Å)	2.8	2.9 (global) /3.9 (focused)
Sharpening B factor (Å <sup>2</sup> )	–57.86	–79.97 (global)/–83.5 (focused)
<b>Coordinate real space refinement</b>		
CC <sub>mask</sub>	0.80	0.80 (focused)
Resolution according to model versus map FSC = 0.5 (masked) criteria (Å)	3.0	4.1 (focused)
Total atoms	146,708	16,722
Protein residues	7,485	1,675
RNA residues	4,019	165
<b>B factors (Å<sup>2</sup>)</b>		
Protein	0.02/67.8/18.2	44.7/647.3/132.9
RNA	0.03/125.4/35.8	74.4/314.2/136.0
Ligand	0.96/68.75/11.81	75.4/87.5/79.8
<b>RMSDs</b>		
Bonds (Å)	0.002	0.002
Angles (°)	0.479	0.421
<b>Validation</b>		
All-atom clashscore	9.39	9.18
MolProbity score	2.05	1.92
<b>Ramachandran plot (%)</b>		
Favored	95.39	97.45
Allowed	4.58	2.55
Outliers	0.04	0
Rotamer outliers	2.02	2.63

EM, electron microscopy; EMD; Electron Microscopy Data Bank; PDB, Pr RMSD, root mean square deviation.

This complex was assembled in the presence of guanosine diphosphate aluminum fluoride (GDP·AlFx), a GTP transition state mimic; however, the SRP54 NG domain was visualized in the GDP state, and the NG domain of SR was not resolved (see [Method details](#)). To capture the distal site interactions, the mammalian RNC·SRP·SR complex was assembled in the presence of 5'-guanylyl imidodiphosphate (GDPNP) ([Figure 1](#); [Table 1](#)). The local resolution of the SRP·SR assembly at the distal site was improved to ~3.6 Å ([Figure S3](#)) compared to 6–7 Å resolution achieved in the previous reconstruction ([Kobayashi et al., 2018](#)). The structures of the SRP targeting complex reveal the

molecular basis of the eukaryotic-specific mechanism of cargo recognition and handover.

### The eukaryotic-specific C terminus of the M domain orients the signal sequence as it emerges from the ribosome

In the early RNC·SRP targeting complex, we resolved the M domain of SRP54 along with the bound signal sequence at an average 3.6 Å resolution ([Figures 2A](#), [S1](#), [S2](#)) positioned next to the NG domain that interacts with uL23 and uL29, as observed previously ([Halic et al., 2006b](#); [Jomaa et al., 2016](#); [Voorhees and](#)

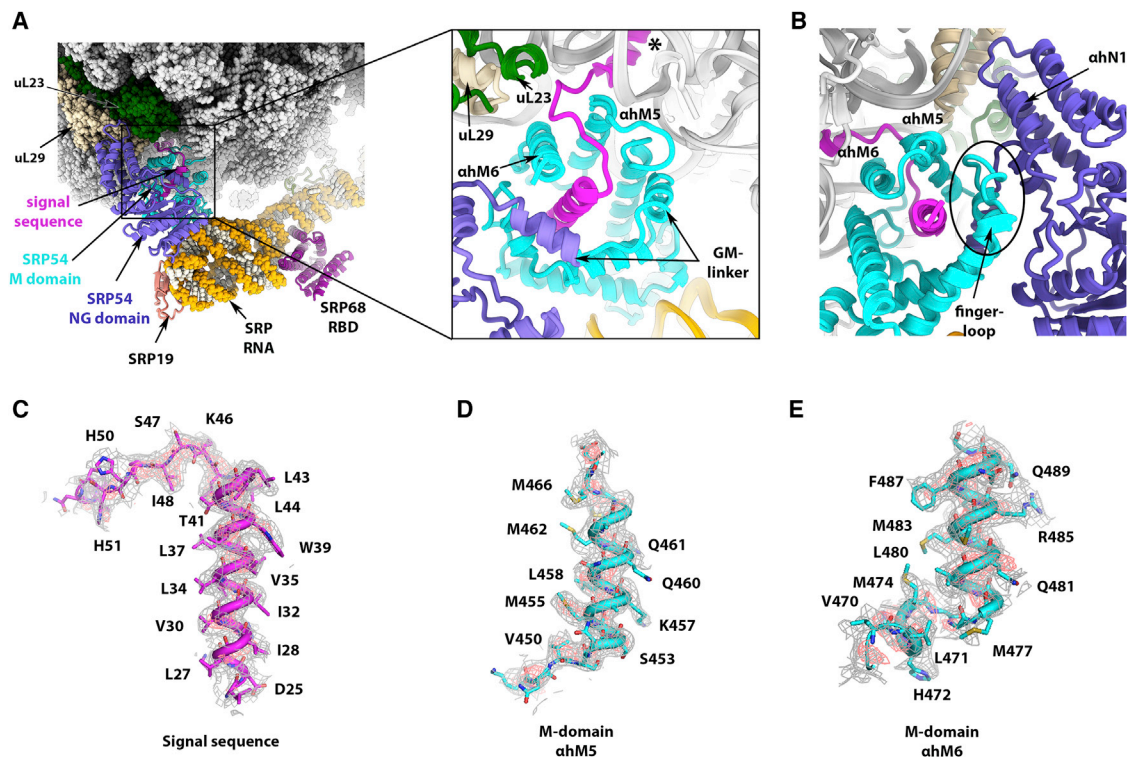


**Figure 2. Molecular interactions between the eukaryotic C-terminal region of SRP54 M domain and the emerging signal sequence**

(A) Overall view of the high-resolution model of the SRP targeting complex shown as cartoon. The coloring is the same as in Figure 1. Ribosomal protein uL23 and uL29 are olive green and wheat, respectively. The boxed region is a close-up of the molecular interactions spanning the C-terminal region of the SRP54 M domain and the signal sequence shown as a cartoon illustration. The region of the nascent chain that is in the ribosome tunnel is indicated. Asterisk indicates the location of the ribosome tunnel exit.

(B) Close-up of the fingerloop region of the M-domain interacting with the signal sequence and the N-terminal helix,  $\alpha$ hN1, of the NG domain of SRP54. The fingerloop of SRP54 is encircled by a black outline.

(C) Representative EM density of the ER signal sequence (magenta). Numbering of the residues in the signal sequence is based on the sequence of the yeast dipeptidyl aminopeptidase B.

(D and E) Representative EM densities of the C-terminal helices ( $\alpha$ hM5 and  $\alpha$ hM6) of SRP54 M domain with underlying atomic coordinates shown as cartoon illustration and sticks. Cryo-EM densities are low-pass filtered to 3.6 Å resolution.

See also Figures S2 and S4.

Hegde, 2015). Notably, the structure reveals the eukaryotic-specific C-terminal region of SRP54 and its interactions with the signal sequence as it emerges from the ribosome tunnel (Figures 2B–2E and S2). The signal sequence is buried within the binding groove of the M domain as it extensively interacts with the surrounding residues via hydrophobic interactions. The M domain groove is further extended by the GM linker, which connects the NG and M domains (Figure 2A). The fingerloop of the M domain is also well resolved and forms contacts with the bound signal sequence and the NG domain of SRP54 (Figure 2B). Interestingly, the fingerloop is positioned between the signal sequence and the N-terminal helix ( $\alpha$ hN1) of the 4-helical bundle of the NG domain, a structural element that regulates SRP and the SR complex assembly (Neher et al., 2008; Wild et al., 2016). The structure suggests that the fingerloop would be able to influence the conformation of the NG domain to accept the SR NG domain once the M domain binds the signal sequence. These results are also consistent with previous biochemical experiments on the bacterial SRP system, where

the fingerloop stimulates NG-heterodimer assembly at the SRP proximal site (Ariosa et al., 2013). In our structure, we also observe an EM density next to the signal sequence that does not originate from surrounding proteins (Figure S2F). This density could be of a detergent molecule present in the SRP buffer, as a previous study reported that SRP binds and is activated by C12E8, a common detergent added to the SRP purification buffer that acts as a signal peptide mimic (Bradshaw et al., 2009).

Furthermore, the nascent chain that emerges from the ribosome tunnel is bound by the M domain with important contributions by a eukaryotic-specific region on the C terminus of SRP54 that include helices  $\alpha$ hM5 and  $\alpha$ hM6 (Figures 2C–2E and S4A). This interaction suggests that these C-terminal helices are involved in guiding and orienting the signal sequence as it exits from the tunnel. In particular, the signal sequence, as established based on maps that reveal the side-chain features and connectivity with the nascent chain in the tunnel, has a different orientation to what was previously observed (Figure S4B), including bacterial SRP complexes (Jomaa et al., 2017), the mammalian

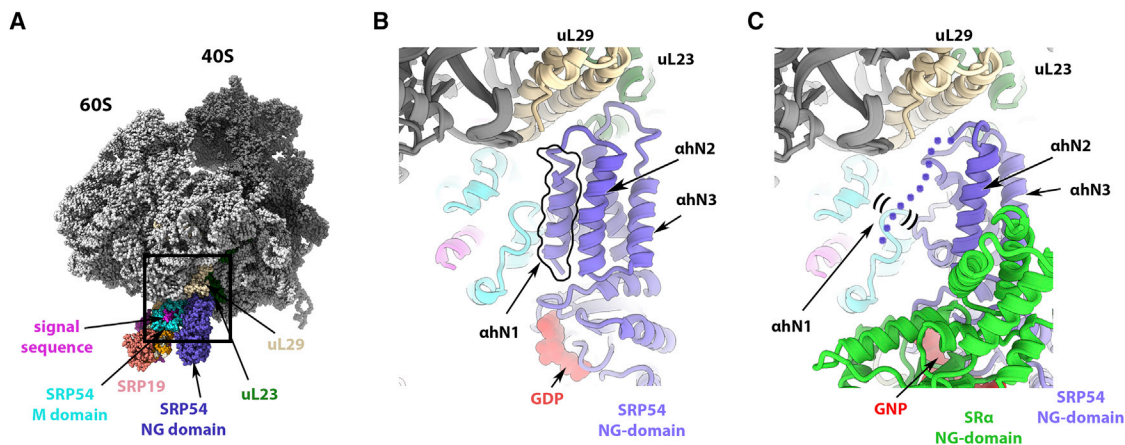


**Figure 3. Model of the SRP-SR NG detachment from the proximal site of the SRP RNA**

(A) Left panel depicts an overview of the structure of the mammalian early RNC-SRP targeting complex shown as spheres.

(B) Close-up of the SRP N domains as observed in the early RNC-SRP targeting complex with all 4  $\alpha$ -helical elements resolved ( $\alpha$ hN1–4) and tightly packed.  $\alpha$ hN1 of SRP54 is indicated by a black outline.

(C) Close-up of the NG-heterodimer as observed in the RNC-SRP-SR complex superimposed onto the early RNC-SRP targeting complex, using the NG domain of SRP54 as a reference.  $\alpha$ hN1 is flexibly disposed in the SRP-SR complex and is indicated by dashed lines. The coloring scheme is the same as in Figure 1. GDP and GNP molecules are shown as spheres and colored red.

The boxed region in (A) indicates the close-up views in (B) and (C) relative to the ribosome.

See also Figures S2 and S5.

RNC-SRP complex (Voorhees and Hegde, 2015), archaeal complexes (Hainzl et al., 2011; Janda et al., 2010) and the bacterial co-translational targeting RNC-SecA complex (Wang et al., 2019). Therefore, these results will have interesting implications for future investigations of the mechanism of signal sequence handover to the translocon.

#### $\alpha$ hN1 of SRP54 modulates NG domain detachment from the proximal site

It remains unclear what causes the NG domain of SRP54 to detach from the vicinity of the ribosome tunnel. The cryo-EM structures of early and late protein targeting states allow us to compare the conformations and molecular features of the SRP54 NG domains. To this end, we compared the structures of the NG domain when it is bound to the surface of the ribosome in the RNC-SRP complex and when it is detached from the proximal binding site, as observed in the SRP-SR complex (Figures 3A–3C). In the ribosome-bound early complex, the NG-domain contains a 4-helical bundle where  $\alpha$ hN1 is visible and packed against  $\alpha$ hN2–4 and where 2 loops located between helices mediate contacts with ribosomal proteins uL23 and uL29. When the NG-heterodimer is formed, the N-terminal  $\alpha$  helix ( $\alpha$ hN1) of SRP54 becomes unstructured, which would weaken interactions with the ribosome. Notably, it was previously reported that truncations of both  $\alpha$ hN1 of bacterial SRP and SR proteins seem to accelerate the SRP-SR complex assembly (Neher et al., 2008), and more recent studies indicated an increased flexibility in  $\alpha$ hN1 in human SRP54 upon complex formation (Juaira et al., 2021; Wild et al., 2016). Therefore, our structures suggest that upon NG heterodimer formation,  $\alpha$ hN1 and adjacent loops are destabilized, which in turn weakens the interaction of SRP54 with the ribosomal surface and thus causes detachment of the SRP54 NG domains from the proximal site.

#### Domains of SRP68 and SR regulate targeting by binding to the distal site of SRP RNA

The map of the late SRP-SR targeting complex docked at the SRP RNA distal site and in the cargo prehandover state was improved locally to an average 3.9 Å resolution (4.1 Å resolution for model versus map based on 0.5 cutoff criteria) by first subtracting the signal of the ribosome and then performing 3-dimensional (3D) alignments focused on the SRP RNA (Figures S3 and S5). The improved resolution of the cryo-EM map allowed the building of atomic models of all of the individual components of this complex to reveal the molecular interactions at side-chain resolution (Figures 4A and S5). As compared to the early SRP complex, in the late SRP-SR complex, the M domain is detached from the ribosome surface and is consequently less resolved with a weak density for the signal sequence. In particular,  $\alpha$ hM5 and  $\alpha$ hM6, and the fingerloop are flexibly disposed and not resolved. At the SRP distal site, however, the improved maps reveal the structure of the second tetratricopeptide repeat (TPR)-like domain of SRP68 (hereafter referred to as RBD2) (Figures S5E and S6A) at the distal site of SRP RNA. RBD2 is structurally similar to the Bro1 TPR-like domain of Alix (Fisher et al., 2007), a protein involved in the endocytic targeting pathway (Figure S6C). Together, the two RBD domains of SRP68 form a butterfly-shaped structure that is pseudo-symmetric (Figure S6A). In contrast to SRP68 RBD, which is anchored to the SRP RNA (Grotwinkel et al., 2014), and thus was visualized in both SRP complexes, RBD2 is flexibly disposed in the early RNC-SRP complex (Figures 1A and 1B). In the SRP-SR complex, however, RBD2 is stabilized via interactions with components of the SR complex (SR $\alpha$  X and NG domains and SR $\beta$ ) and contacts with the SRP RNA at the connection between the S domain and the Alu domain (Figure S6D). Consequently, RBD2 rigidifies the relative

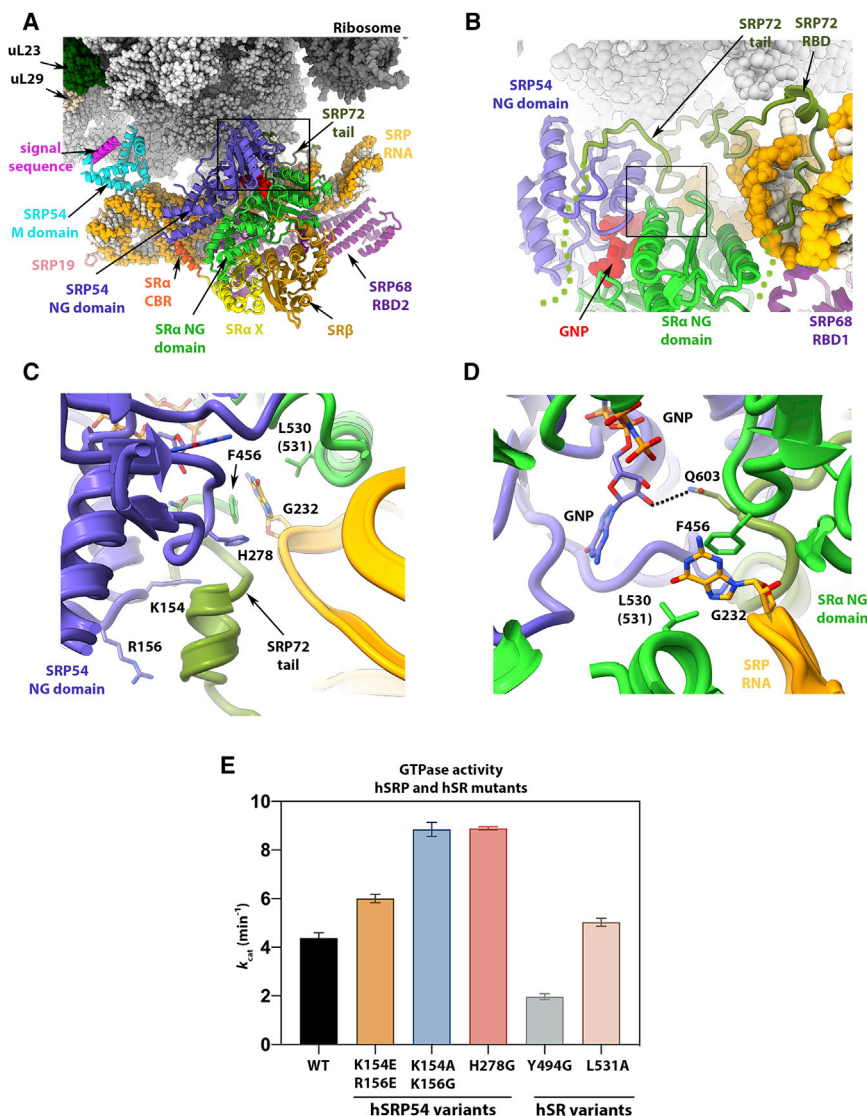


**Figure 4. Molecular interactions between SRP72, SRP RNA, and the NG-heterodimer at the distal site in the SRP-SR complex**

(A) Overall view of the high-resolution model of the SRP-SR targeting complex. The coloring is same as in Figure 1. Ribosomal protein uL23 and uL29 are olive green and wheat, respectively. GDPNP molecules are shown as spheres and colored red. (B) Close-up of the SRP72 RBD and SRP72 C-terminal tail interactions with SRP RNA and the NG-heterodimer. The C-terminal tail of SRP72 interacting with SRP54 is labeled. Dashed lines indicate the regions that are flexible in the cryo-EM map. GDPNP molecules are shown as spheres and colored red.

(C) Surveillance of the SRP72 and SRP RNA G232 insertion into the GTPases interface by SRP54 and SR $\alpha$  (green) G domains. SRP54 residues H278, K154, and R156, and SR $\alpha$  F456, L530 (hSR L531) are shown as sticks.

(D) Close-up of the Q603 residue of SRP72 inserted into the moiety of the bound GDPNP molecule bound to the SRP54 G domain. The hydrogen bonding distance between Q603 and the 2'OH of the sugar is marked as a dashed black line.

(E) GTPase rate constants of the SRP-SR complex ( $k_{cat}$ ) formed by human SRP (hSRP) and SR $\alpha$  $\beta$ - $\Delta$ TM. Reactions with SRPs bearing indicated SRP54 (h54) mutations or with SR bearing indicated SR $\alpha$  mutations are indicated. All of the measurements were carried out with SRP54 fused to a model signal sequence (Lee et al., 2018) and with the 80S ribosome present. The values of  $k_{cat}$  were derived from analysis of the data shown in Figure S8.

Data were reported as means  $\pm$  SDs, with  $n = 2-4$ . Boxed regions in (A) and (B) indicate the close-up regions in (C) and (D).

See also Figures S5-S8.

disposition between the Alu and S domains of SRP in the cargo prehandover conformation, which could facilitate the dissociation of the Alu domain as the translocon displaces the S domain of the SRP.

The cryo-EM structure of the SRP-SR complex also resolves a conserved linker region of SR $\alpha$ , referred to as CBR, or the channel binding region (Jadhav et al., 2015b) (Figure S5H). The CBR forms a short  $\alpha$ -helical element, rich in positively charged residues, that contacts the SRP RNA (Figures 4A and S6B). CBR was proposed to switch from the post-translational Sec62-dependent to the SRP-dependent mode of targeting by binding the Sec61 translocon and displacing Sec62 (Jadhav et al., 2015b). The binding of CBR on SRP, as observed in the SRP-SR structure, is in close proximity to where the signal sequence is handed over to the translocon and is consistent with the proposed switch mechanism to the SRP-dependent mode.

### Molecular basis for the regulation of SRP-SR GTPase activity

We previously reported that the GTPase activity of the SRP54 and SR $\alpha$  NG-heterodimer is inhibited by the C-terminal tail of SRP72 and by a flipped-out nucleotide of SRP RNA (Kobayashi et al., 2018; Lee et al., 2018). The improved cryo-EM map of the SRP-SR reveals these interactions at the molecular level. First, the universally conserved G232 residue of the SRP RNA along with the C-terminal region of SRP72 interacts with the interface between the 2 GTPase domains of the receptor and SRP54. Second, the C-terminal tail of SRP72 forms a 2-turn  $\alpha$ -helical element and then inserts a highly conserved residue, Gln603, toward the ribose 2'OH group of the GDPNP molecule bound to the SRP54 GTPase domain (Figures 4B-4D and S7). This helical insertion is similar to the previously observed X-ray structure of the bacterial SRP homolog FlhF in complex with an activator helix of the YlxH protein (Bange et al., 2011) (Figure 5). The C-terminal

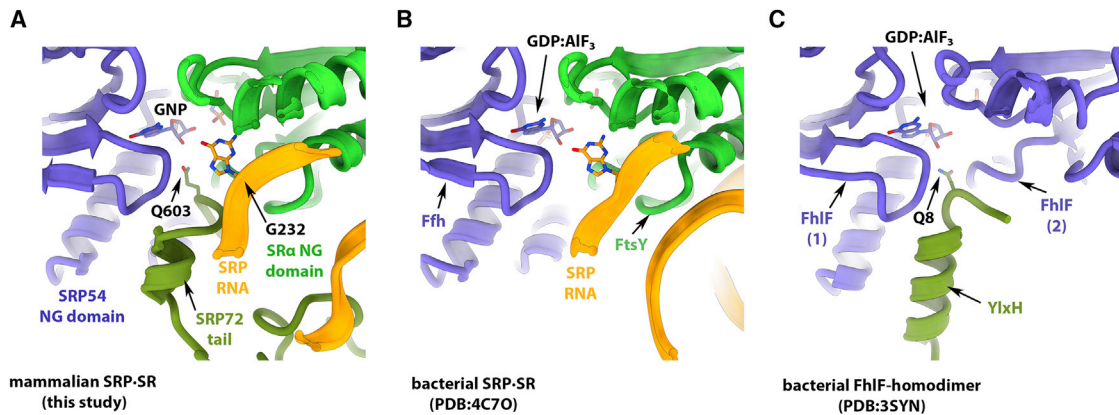


**Figure 5. Molecular evolution of the SRP GTPases from bacteria to mammals**

(A–C) Comparison between the GTPase interface of the SRP and SR receptor-type GTPases and their regulation mechanism in bacteria and in mammals. The bacterial SRP (PDB: 4C70) and SRP-like (PDB: 3SYN) system contain either RNA or protein element that acts as a GTPase activator. The mammalian SRP system evolved to contain both RNA and protein elements, but now act to inhibit GTPase activity instead.

See also Figure S7.

tail of SRP72 further snakes along the surface of SRP54, extending the 6-strand  $\beta$  sheet of the G domain by an additional strand (Figures 4B and S4I). The tail is flexibly disposed following residues D614 and A615 (Figure S7E), where caspase cleaves SRP72 during apoptosis (Becker et al., 2017; Utz et al., 1998). The helical insertion of SRP72 is stabilized through interactions with SRP54 residues His278, Lys154, and Arg156 (Figures 4C and S7B–S7D). We further validated our structural observations by generating human SRP constructs in which these residues are mutated to the opposite charge or into alanine/glycine. Both types of mutations lead to a significant increase in GTP hydrolysis from the SRP·SR complex (Figures 4E and S8). In contrast, the mutation of Tyr493 (hSR Tyr494) in the SR $\alpha$  NG domain (Figure S7D), which appears to be important for stabilizing the geometry of the GTPase fold of the SRP·SR heterodimer, modestly decreased GTPase activity.

Although the insertion of an activator helix of YlxH into the FhlF-homodimer to activate its GTPase activity (Bange et al., 2011) is structurally analogous to the insertion of the C-terminal tail of SRP72 next to the GTP (Figure 5), the 2 features have an opposite effect on the GTPase activity. Similarly, although both bacterial and eukaryotic SRP RNA feature a universally conserved flipped-out RNA base that is inserted into the SRP·SR GTPase interface (Becker et al., 2017; Jomaa et al., 2017; Kobayashi et al., 2018; Voigts-Hoffmann et al., 2013), they appear to have opposite roles in regulating the GTPase activity of SRP and SR. Therefore, our results indicate that the eukaryotic SRP uses both of these structural elements (RNA and protein insertion) to inhibit GTPase activity, possibly by altering the geometry of the GTPase center, which is opposite to what is observed for analogous elements in bacteria.

## DISCUSSION

The cryo-EM structures of the mammalian early SRP and late SRP·SR ribosome complexes reveal the structural basis of membrane targeting in the eukaryotic SRP pathway. Both early

and late events of SRP targeting in mammals are regulated primarily by eukaryotic-specific protein elements, which replace and extend the roles that SRP RNA is responsible for in the bacterial system. Specifically, we were able to dissect the molecular mechanism and interactions that govern nascent chain recognition in the early phases of targeting to the ER membrane and GTPase regulation before and during cargo handover (Figure 6). In summary, SRP binds and recognizes the ribosome with a nascent polypeptide chain to be targeted to the membrane. Previous data indicated that SRP first binds the ribosome to scan for the signal sequence before it emerges from the exit tunnel (Bornemann et al., 2008; Chartron et al., 2016; Denks et al., 2017; Jomaa et al., 2016; Voorhees and Hegde, 2015). Our structures of the early protein targeting complexes provide the structural basis for the interactions between the eukaryotic C-terminal region ( $\alpha$ hM5 and  $\alpha$ hM6) of the SRP54 M domain and the nascent chain. This interaction suggests that the SRP orients the signal sequence as it exits the ribosome tunnel. After cargo recognition, the ribosome and SRP complex are delivered to the ER membrane facilitated by interactions with SR. Our results indicate that a conformational change in  $\alpha$ hN1 of the SRP54 NG domain is induced upon SRP·SR complex assembly. This conformational change displaces the loops in SRP54 NG domain, causing its detachment from the ribosome. After the NG-heterodimer translocates to the SRP RNA distal site, the M domain of SRP54 exposes the signal sequence for cargo handover to the Sec translocon, as seen here in the RNC·SRP·SR complex (Figure 6).

The RNC·SRP·SR complex resolves SRP and SR at the distal site of the SRP RNA. In the current improved structure, we visualized the second TPR-like domain of SRP68, RBD2, and the CBR of the SR $\alpha$  linker region interacting with the SRP RNA. The positioning of these elements at functionally important regions of the SRP RNA suggests a possible role in conformational changes that accompany membrane docking and in recruitment of the Sec translocon. The docking of the SRP·SR NG-heterodimer and the eukaryotic-specific SRX/ $\beta$ -heterodimer at the

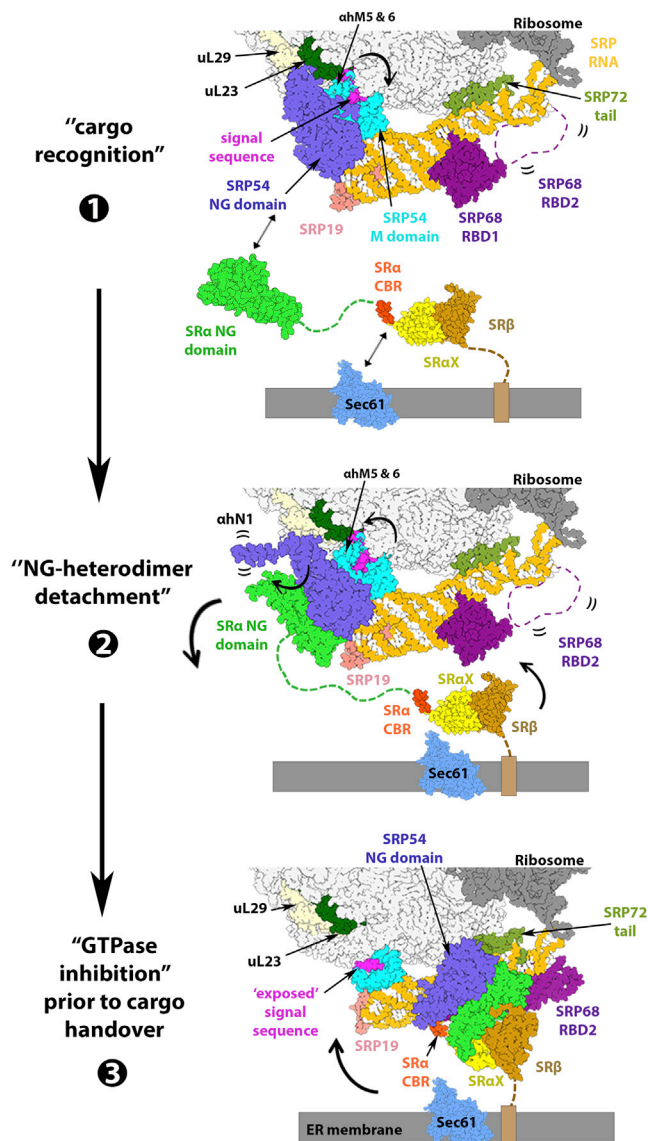


**Figure 6. Mechanism of cargo recognition and GTPase regulation in the mammalian SRP targeting pathway**

Schematic of the eukaryotic SRP pathway in mammals highlighting the stages of cargo recognition, NG-heterodimer detachment, and GTPase inhibition before cargo handover. The cargo is first recognized and guided as it emerges from the ribosome tunnel by the C-terminal region of the SRP54. SRP NG-heterodimer formation leads to a conformational change in the SRP54 NG domain, displacing it from the ribosome, which accelerates the NG-heterodimer repositioning to the distal site of the SRP RNA. The positioning of the SRP68 RBD2 and SR $\alpha$  CBR at functionally important regions of SRP RNA suggests their role in conformational changes that accompany membrane docking and in the recruitment of the translocon, respectively. The SRP72 inserts a highly conserved residue Q603 together with the residue G232 of the SRP RNA into the NG-heterodimer GTPase interface of SRP and SR to inhibit GTPase activity. At this stage, the exposed signal sequence bound to the M domain of SRP54 will be handed over to the Sec translocon on the ER membrane. Curved arrows indicate conformational changes.

distal site involves the insertion of a highly conserved residue, Gln603, of SRP72 in the GTPase interface to regulate its activity. The insertion of this residue, in addition to G232 of the SRP RNA, into the SRP·SR GTPases interface is reminiscent of 2 bacterial elements that in different systems independently stimulate SRP·SR GTPase activity. It is intriguing that in the eukaryotic SRP system, these elements inhibit the SRP·SR GTPase activity. It is not clear why SRP evolved in such a direction. A possible explanation is that the GTPase inhibition enables SRP to carry out multiple rounds of targeting reactions for ribosomes translating on the same mRNA, before GTP is hydrolyzed. Interestingly, previous studies have shown ribosomes bound to the ER Sec translocon in an SR-independent manner (Potter and Nicchitta, 2000). Another possibility is that GTP hydrolysis is delayed to allow full engagement between the signal sequence and the Sec translocon before SRP is released from the ER. Our results provide opportunities to investigate canonical and non-canonical mechanisms of the SRP targeting process that exist in eukaryotic systems.

## STAR★METHODS

Detailed methods are provided in the online version of this paper and include the following:

- KEY RESOURCES TABLE
- RESOURCE AVAILABILITY
  - Lead contact
  - Materials availability
  - Data and code availability
- EXPERIMENTAL MODEL AND SUBJECT DETAILS
- METHOD DETAILS
  - Preparation of mammalian ribosome nascent chain complexes
  - Purification of recombinant human SRP and SR and GTPase activity assays
  - Cryo-EM sample preparation
  - Data processing
  - Model building
- QUANTIFICATION AND STATISTICAL ANALYSIS

## SUPPLEMENTAL INFORMATION

Supplemental information can be found online at <https://doi.org/10.1016/j.celrep.2021.109350>.

## ACKNOWLEDGMENTS

We thank A. Scaiola and D. Boehringer for the support with EM data processing, M. Leibundgut for the support with model building, and Jae Ho Lee and members of the Ban and Shan groups for discussions and comments on the manuscript. Cryo-EM data were collected at the Scientific Center for Optical and Electron Microscopy at the ETH Zurich (ScopeM). We gratefully acknowledge the support of NVIDIA Corporation for the Titan Xp GPU used in this research through a GPU Grant program awarded to A.J. This work was supported by the Swiss National Science Foundation (SNSF) (grant no. 310030B\_163478); the National Center of Excellence in Research (NCCR) RNA & Disease Program of the SNSF (grant no. 51NF40\_141735), to N.B.; and National Institutes of Health grant GM107368, National Science

Foundation grant MCB-1929452, and the Gordon and Betty Moore Foundation through grant GBMF2939 to S.S.

#### AUTHOR CONTRIBUTIONS

A.J., N.B., and S.S. conceived the project. K.K. and A.J. prepared samples for the cryo-EM analysis. A.J. collected the cryo-EM data. A.J. and S.E. performed the reconstruction and model building. S.C. and Z.Z. purified the recombinant human SRP, SR, and performed the biochemical experiments. N.B., S.S., and A.J. supervised the research. A.J., N.B., and S.S. wrote the manuscript. All of the authors interpreted the data and contributed to the final versions of the manuscript.

#### DECLARATION OF INTERESTS

The authors declare no competing interests. N.B. is a member of the *Cell Reports* advisory board.

Received: December 21, 2020

Revised: April 23, 2021

Accepted: June 15, 2021

Published: July 13, 2021

#### REFERENCES

- Adams, P.D., Afonine, P.V., Bunkóczy, G., Chen, V.B., Davis, I.W., Echols, N., Headd, J.J., Hung, L.-W., Kapral, G.J., Grosse-Kunstleve, R.W., et al. (2010). *PHENIX*: a comprehensive Python-based system for macromolecular structure solution. *Acta Crystallogr. D Biol. Crystallogr.* **66**, 213–221.
- Akopian, D., Shen, K., Zhang, X., and Shan, S.O. (2013). Signal recognition particle: an essential protein-targeting machine. *Annu. Rev. Biochem.* **82**, 693–721.
- Ariosa, A.R., Duncan, S.S., Saraogi, I., Lu, X., Brown, A., Phillips, G.J., and Shan, S.-O. (2013). Fingerloop activates cargo delivery and unloading during cotranslational protein targeting. *Mol. Biol. Cell* **24**, 63–73.
- Bange, G., Kümmerer, N., Grudnik, P., Lindner, R., Petzold, G., Kressler, D., Hurt, E., Wild, K., and Sinning, I. (2011). Structural basis for the molecular evolution of SRP-GTPase activation by protein. *Nat. Struct. Mol. Biol.* **18**, 1376–1380.
- Becker, M.M.M., Lapouge, K., Segnitz, B., Wild, K., and Sinning, I. (2017). Structures of human SRP72 complexes provide insights into SRP RNA remodeling and ribosome interaction. *Nucleic Acids Res.* **45**, 470–481.
- Bellanné-Chantelot, C., Schmaltz-Panneau, B., Marty, C., Fenneteau, O., Callébaud, I., Clauin, S., Docet, A., Damaj, G.-L., Leblanc, T., Pellier, I., et al. (2018). Mutations in the *SRP54* gene cause severe congenital neutropenia as well as Shwachman-Diamond-like syndrome. *Blood* **132**, 1318–1331.
- Bornemann, T., Jöckel, J., Rodnina, M.V., and Wintermeyer, W. (2008). Signal sequence-independent membrane targeting of ribosomes containing short nascent peptides within the exit tunnel. *Nat. Struct. Mol. Biol.* **15**, 494–499.
- Bradshaw, N., Neher, S.B., Booth, D.S., and Walter, P. (2009). Signal sequences activate the catalytic switch of SRP RNA. *Science* **323**, 127–130.
- Chartron, J.W., Hunt, K.C.L., and Frydman, J. (2016). Cotranslational signal-independent SRP preloading during membrane targeting. *Nature* **536**, 224–228.
- D'Altri, T., Schuster, M.B., Wenzel, A., and Porse, B.T. (2019). Heterozygous loss of *Srp72* in mice is not associated with major hematological phenotypes. *Eur. J. Haematol.* **103**, 319–328.
- Denks, K., Sliwinski, N., Erichsen, V., Borodkina, B., Origi, A., and Koch, H.-G. (2017). The signal recognition particle contacts uL23 and scans substrate translation inside the ribosomal tunnel. *Nat. Microbiol.* **2**, 16265.
- Draycheva, A., Bornemann, T., Ryazanov, S., Lakomek, N.A., and Wintermeyer, W. (2016). The bacterial SRP receptor, FtsY, is activated on binding to the translocon. *Mol. Microbiol.* **102**, 152–167.
- Emsley, P., and Cowtan, K. (2004). *Coot*: model-building tools for molecular graphics. *Acta Crystallogr. D Biol. Crystallogr.* **60**, 2126–2132.
- Fisher, R.D., Chung, H.-Y., Zhai, Q., Robinson, H., Sundquist, W.I., and Hill, C.P. (2007). Structural and biochemical studies of ALIX/AIP1 and its role in retrovirus budding. *Cell* **128**, 841–852.
- Gilmore, R., Blobel, G., and Walter, P. (1982a). Protein translocation across the endoplasmic reticulum. I. Detection in the microsomal membrane of a receptor for the signal recognition particle. *J. Cell Biol.* **95**, 463–469.
- Gilmore, R., Walter, P., and Blobel, G. (1982b). Protein translocation across the endoplasmic reticulum. II. Isolation and characterization of the signal recognition particle receptor. *J. Cell Biol.* **95**, 470–477.
- Goddard, T.D., Huang, C.C., Meng, E.C., Pettersen, E.F., Couch, G.S., Morris, J.H., and Ferrin, T.E. (2018). UCSF ChimeraX: meeting modern challenges in visualization and analysis. *Protein Sci.* **27**, 14–25.
- Görlich, D., and Rapoport, T.A. (1993). Protein translocation into proteoliposomes reconstituted from purified components of the endoplasmic reticulum membrane. *Cell* **75**, 615–630.
- Grotwinkel, J.T., Wild, K., Segnitz, B., and Sinning, I. (2014). SRP RNA remodeling by SRP68 explains its role in protein translocation. *Science* **344**, 101–104.
- Hainzl, T., Huang, S., Meriläinen, G., Brännström, K., and Sauer-Eriksson, A.E. (2011). Structural basis of signal-sequence recognition by the signal recognition particle. *Nat. Struct. Mol. Biol.* **18**, 389–391.
- Halic, M., Gartmann, M., Schlenker, O., Mielke, T., Pool, M.R., Sinning, I., and Beckmann, R. (2006a). Signal recognition particle receptor exposes the ribosomal translocon binding site. *Science* **312**, 745–747.
- Halic, M., Blau, M., Becker, T., Mielke, T., Pool, M.R., Wild, K., Sinning, I., and Beckmann, R. (2006b). Following the signal sequence from ribosomal tunnel exit to signal recognition particle. *Nature* **444**, 507–511.
- Hwang Fu, Y.-H., Huang, W.Y.C., Shen, K., Groves, J.T., Miller, T., and Shan, S.O. (2017). Two-step membrane binding by the bacterial SRP receptor enable efficient and accurate co-translational protein targeting. *eLife* **6**, e25885.
- Hwang Fu, Y.-H., Chandrasekar, S., Lee, J.H., and Shan, S.O. (2019). A molecular recognition feature mediates ribosome-induced SRP-receptor assembly during protein targeting. *J. Cell Biol.* **218**, 3307–3319.
- Jadhav, B., Wild, K., Pool, M.R., and Sinning, I. (2015a). Structure and Switch Cycle of SRP as Ancestral Eukaryotic GTPase Associated with Secretory Membranes. *Structure* **23**, 1838–1847.
- Jadhav, B., McKenna, M., Johnson, N., High, S., Sinning, I., and Pool, M.R. (2015b). Mammalian SRP receptor switches the Sec61 translocase from Sec62 to SRP-dependent translocation. *Nat. Commun.* **6**, 10133.
- Janda, C.Y., Li, J., Oubridge, C., Hernández, H., Robinson, C.V., and Nagai, K. (2010). Recognition of a signal peptide by the signal recognition particle. *Nature* **465**, 507–510.
- Jiang, Y., Cheng, Z., Mandon, E.C., and Gilmore, R. (2008). An interaction between the SRP receptor and the translocon is critical during cotranslational protein translocation. *J. Cell Biol.* **180**, 1149–1161.
- Jomaa, A., Boehringer, D., Leibundgut, M., and Ban, N. (2016). Structures of the *E. coli* translating ribosome with SRP and its receptor and with the translocon. *Nat. Commun.* **7**, 10471.
- Jomaa, A., Fu, Y.-H.H., Boehringer, D., Leibundgut, M., Shan, S.O., and Ban, N. (2017). Structure of the quaternary complex between SRP, SR, and translocon bound to the translating ribosome. *Nat. Commun.* **8**, 15470.
- Juaire, K.D., Lapouge, K., Becker, M.M.M., Kotova, I., Michelhans, M., Carapito, R., Wild, K., Bahram, S., and Sinning, I. (2021). Structural and Functional Impact of SRP54 Mutations Causing Severe Congenital Neutropenia. *Structure* **29**, 15–28.e7.
- Kelley, L.A., Mezulis, S., Yates, C.M., Wass, M.N., and Sternberg, M.J.E. (2015). The Phyre2 web portal for protein modeling, prediction and analysis. *Nat. Protoc.* **10**, 845–858.
- Kirwan, M., Walne, A.J., Plagnol, V., Velangi, M., Ho, A., Hossain, U., Vulliamy, T., and Dokal, I. (2012). Exome sequencing identifies autosomal-dominant SRP72 mutations associated with familial aplasia and myelodysplasia. *Am. J. Hum. Genet.* **90**, 888–892.

- Kobayashi, K., Jomaa, A., Lee, J.H., Chandrasekar, S., Boehringer, D., Shan, S.O., and Ban, N. (2018). Structure of a prehandover mammalian ribosomal SRP-SRP receptor targeting complex. *Science* **360**, 323–327.
- Konantz, M., Schürch, C., Müller, J.S., Schärer, J., Carapito, R., Bahram, S., and Lengerke, C. (2018). Mutation-Specific Dose Reduction in Functional SRP54 Protein Causes Isolated or Syndromic Neutropenia with Shwachman-Diamond-like Features. *Blood* **132**, 1300.
- Lee, J.H., Chandrasekar, S., Chung, S., Hwang Fu, Y.-H., Liu, D., Weiss, S., and Shan, S. (2018). Sequential activation of human signal recognition particle by the ribosome and signal sequence drives efficient protein targeting. *Proc. Natl. Acad. Sci.* **115**, E5487–E5496.
- Mandon, E.C., Jiang, Y., and Gilmore, R. (2003). Dual recognition of the ribosome and the signal recognition particle by the SRP receptor during protein targeting to the endoplasmic reticulum. *J. Cell Biol.* **162**, 575–585.
- Miller, J.D., Tajima, S., Lauffer, L., and Walter, P. (1995). The beta subunit of the signal recognition particle receptor is a transmembrane GTPase that anchors the alpha subunit, a peripheral membrane GTPase, to the endoplasmic reticulum membrane. *J. Cell Biol.* **128**, 273–282.
- Neher, S.B., Bradshaw, N., Floor, S.N., Gross, J.D., and Walter, P. (2008). SRP RNA controls a conformational switch regulating the SRP-SRP receptor interaction. *Nat. Struct. Mol. Biol.* **15**, 916–923.
- Nyathi, Y., Wilkinson, B.M., and Pool, M.R. (2013). Co-translational targeting and translocation of proteins to the endoplasmic reticulum. *Biochim. Biophys. Acta* **1833**, 2392–2402.
- Park, E., and Rapoport, T.A. (2012). Mechanisms of Sec61/SecY-mediated protein translocation across membranes. *Annu. Rev. Biophys.* **41**, 21–40.
- Peluso, P., Shan, S.O., Nock, S., Herschlag, D., and Walter, P. (2001). Role of SRP RNA in the GTPase cycles of Ffh and FtsY. *Biochemistry* **40**, 15224–15233.
- Pettersen, E.F., Goddard, T.D., Huang, C.C., Couch, G.S., Greenblatt, D.M., Meng, E.C., and Ferrin, T.E. (2004). UCSF Chimera—a visualization system for exploratory research and analysis. *J. Comput. Chem.* **25**, 1605–1612.
- Pfeffer, S., Dudek, J., Schaffer, M., Ng, B.G., Albert, S., Plitzko, J.M., Baumeister, W., Zimmermann, R., Freeze, H.H., Engel, B.D., and Förster, F. (2017). Dissecting the molecular organization of the translocon-associated protein complex. *Nat. Commun.* **8**, 14516.
- Potter, M.D., and Nicchitta, C.V. (2000). Regulation of ribosome detachment from the mammalian endoplasmic reticulum membrane. *J. Biol. Chem.* **275**, 33828–33835.
- Schwartz, T., and Blobel, G. (2003). Structural basis for the function of the  $\beta$  subunit of the eukaryotic signal recognition particle receptor. *Cell* **112**, 793–803.
- Tajima, S., Lauffer, L., Rath, V.L., and Walter, P. (1986). The signal recognition particle receptor is a complex that contains two distinct polypeptide chains. *J. Cell Biol.* **103**, 1167–1178.
- Utz, P.J., Hottel, M., Le, T.M., Kim, S.J., Geiger, M.E., van Venrooij, W.J., and Anderson, P. (1998). The 72-kDa component of signal recognition particle is cleaved during apoptosis. *J. Biol. Chem.* **273**, 35362–35370.
- Voigts-Hoffmann, F., Schmitz, N., Shen, K., Shan, S.O., Ataïde, S.F., and Ban, N. (2013). The structural basis of FtsY recruitment and GTPase activation by SRP RNA. *Mol. Cell* **52**, 643–654.
- Voorhees, R.M., and Hegde, R.S. (2015). Structures of the scanning and engaged states of the mammalian SRP-ribosome complex. *eLife* **4**, e07975.
- Voorhees, R.M., and Hegde, R.S. (2016). Structure of the Sec61 channel opened by a signal sequence. *Science* **351**, 88–91.
- Voorhees, R.M., Fernández, I.S., Scheres, S.H.W., and Hegde, R.S. (2014). Structure of the mammalian ribosome-Sec61 complex to 3.4 Å resolution. *Cell* **157**, 1632–1643.
- Wang, S., Jomaa, A., Jaskolowski, M., Yang, C.-I., Ban, N., and Shan, S.O. (2019). The molecular mechanism of cotranslational membrane protein recognition and targeting by SecA. *Nat. Struct. Mol. Biol.* **26**, 919–929.
- Wild, K., Bange, G., Motiejunas, D., Kribelbauer, J., Hendricks, A., Segnitz, B., Wade, R.C., and Sinning, I. (2016). Structural Basis for Conserved Regulation and Adaptation of the Signal Recognition Particle Targeting Complex. *J. Mol. Biol.* **428**, 2880–2897.
- Wild, K., Juaira, K.D., Soni, K., Shanmuganathan, V., Hendricks, A., Segnitz, B., Beckmann, R., and Sinning, I. (2019). Reconstitution of the human SRP system and quantitative and systematic analysis of its ribosome interactions. *Nucleic Acids Res.* **47**, 3184–3196.
- Young, J.C., Ursini, J., Legate, K.R., Miller, J.D., Walter, P., and Andrews, D.W. (1995). An amino-terminal domain containing hydrophobic and hydrophilic sequences binds the signal recognition particle receptor  $\alpha$  subunit to the  $\beta$  subunit on the endoplasmic reticulum membrane. *J. Biol. Chem.* **270**, 15650–15657.
- Zhang, K. (2016). Gctf: real-time CTF determination and correction. *J. Struct. Biol.* **193**, 1–12.
- Zhang, X., and Shan, S.O. (2014). Fidelity of cotranslational protein targeting by the signal recognition particle. *Annu. Rev. Biophys.* **43**, 381–408.
- Zheng, S.Q., Palovcak, E., Armache, J.-P., Verba, K.A., Cheng, Y., and Agard, D.A. (2017). MotionCor2: anisotropic correction of beam-induced motion for improved cryo-electron microscopy. *Nat. Methods* **14**, 331–332.
- Zivanov, J., Nakane, T., Forsberg, B.O., Kimanius, D., Hagen, W.J., Lindahl, E., and Scheres, S.H. (2018). New tools for automated high-resolution cryo-EM structure determination in RELION-3. *eLife* **7**, e42166.

STAR★METHODS

KEY RESOURCES TABLE

REAGENT or RESOURCE	SOURCE	IDENTIFIER
<b>Antibodies</b>		
ANTI-FLAG® M2 Affinity Gel	SIGMA	F3165
<b>Bacterial strains</b>		
<i>E. coli</i> BL21- DE3	NEB	C2527H
<i>E. coli</i> BL21 S1 pRARE	Life Technologies	11665
<b>Biological samples</b>		
Flexi® Rabbit Reticulocyte Lysate System	Promega	L4540
Canine SRP	tRNA probes	N/A
Sec61p from pancreatic pig microsomes	<a href="#">Kobayashi et al., 2018</a>	N/A
80S ribosome (Rabbit)	<a href="#">Lee et al., 2018</a>	N/A
<b>Chemicals, peptides, and recombinant proteins</b>		
3 × FLAG® Peptide	SIGMA	F4799
Digitonin	SIGMA	D141
GDPNP (Guanosine 5'-[β,γ-imido]triphosphate)	SIGMA	G0635
GDP (Guanosine 5'-diphosphate)	SIGMA	G7127
GTP (Guanosine 5'-triphosphate lithium salt)	SIGMA	G5884
γ-32P-GTP	Perkin Elmer	BLU004Z250UC
Recombinant rabbit SR	<a href="#">Kobayashi et al., 2018</a>	N/A
Recombinant human SRP	<a href="#">Lee et al., 2018</a>	N/A
Recombinant human SR	<a href="#">Lee et al., 2018</a>	N/A
Copper Grids R2/2	Quantifoil	N/A
<b>Deposited data</b>		
Cryo-EM map of RNC·SRP·SR	this study	EMD-12800
Cryo-EM structure of SRP·SR, distal site	this study	PDB ID 7OBQ, EMD-12799
Cryo-EM structure of the early RNC·SRP	this study	PDB ID 7OBR, EMD-12801
<b>Recombinant DNA</b>		
pUC57-SS-SH	<a href="#">Kobayashi et al., 2018</a>	N/A
pET20b-SRα	<a href="#">Kobayashi et al., 2018</a>	N/A
pET24a-SRβ	<a href="#">Kobayashi et al., 2018</a>	N/A
<b>Software and algorithms</b>		
RELION3	<a href="#">Zivanov et al., 2018</a>	<a href="https://www3.mrc-lmb.cam.ac.uk/relion/index.php?title=Main_Page">https://www3.mrc-lmb.cam.ac.uk/relion/index.php?title=Main_Page</a>
USCF CHIMERA	<a href="#">Pettersen et al., 2004</a>	<a href="https://www.cgl.ucsf.edu/chimera/">https://www.cgl.ucsf.edu/chimera/</a>
PHYRE2	<a href="#">Kelley et al., 2015</a>	<a href="http://www.sbg.bio.ic.ac.uk/~phyre2/html/page.cgi?id=index">http://www.sbg.bio.ic.ac.uk/~phyre2/html/page.cgi?id=index</a>
COOT	<a href="#">Emsley and Cowtan, 2004</a>	<a href="https://www2.mrc-lmb.cam.ac.uk/personal/pemsley/coot/">https://www2.mrc-lmb.cam.ac.uk/personal/pemsley/coot/</a>
PHENIX	<a href="#">Adams et al., 2010</a>	<a href="https://phenix-online.org/documentation/reference/refinement.html">https://phenix-online.org/documentation/reference/refinement.html</a>
ChimeraX	<a href="#">Goddard et al., 2018</a>	<a href="https://www.rbvi.ucsf.edu/chimerax/">https://www.rbvi.ucsf.edu/chimerax/</a>
PyMOL	Schrodinger	<a href="https://pymol.org/2/">https://pymol.org/2/</a>
MotionCor2	<a href="#">Zheng et al., 2017</a>	<a href="https://emcore.ucsf.edu/ucsf-software">https://emcore.ucsf.edu/ucsf-software</a>
GCTF	<a href="#">Zhang, 2016</a>	<a href="https://www2.mrc-lmb.cam.ac.uk/research/locally-developed-software/zhang-software/">https://www2.mrc-lmb.cam.ac.uk/research/locally-developed-software/zhang-software/</a>

## RESOURCE AVAILABILITY

### Lead contact

Further information and requests for resources and reagents should be directed to and will be fulfilled by the Lead Contact, Nenad Ban ([ban@mol.biol.ethz.ch](mailto:ban@mol.biol.ethz.ch)).

### Materials availability

Plasmids used in this study are available from the Lead Contact upon request. This study did not generate new unique reagents.

### Data and code availability

Cryo-EM maps and model coordinates are deposited in the EMDB as EMD-12799 and EMD-12800, EMD-12801 and in the PDB as PDB ID 7OBQ, and PDB ID 7OBR.

## EXPERIMENTAL MODEL AND SUBJECT DETAILS

For protein expression, bacterial strains *Escherichia coli* BL21 were used. Translating ribosomes were isolated from rabbit reticulocyte lysate system using an *in-vitro* translation system. Targeting complexes were then reconstituted using purified endogenous and recombinant components that are listed in the [Key resources table](#).

## METHOD DETAILS

### Preparation of mammalian ribosome nascent chain complexes

The plasmid pUC57 plasmid (GenScript) containing a 3x FLAG tag followed by 65 amino acids of the yeast Dipeptidyl aminopeptidase B protein containing the signal sequence VGILVLLIWTGTVLLL was linearized by PstI and then mRNA was generated by *in vitro* transcription using the T7 polymerase ([Kobayashi et al., 2018](#)). The transcribed mRNA was translated in the Flexi® Rabbit Reticulocyte Lysate System (Promega) at concentration of 214 ng/μL for 25 minutes at 32°C to generate run-off ribosome nascent chain complexes. For the purification of RNCs, 0.5 mL of ANTI-FLAG® M2 Affinity Gel (SIGMA-ALDRICH) previously washed with buffer A (50 mM HEPES-KOH, pH 7.6, 100 mM KCl, 5 mM MgCl<sub>2</sub>) was added to 4.7 mL of the translation reaction product and incubated for 2 hours at 4°C. Following the removal of the lysate, the gel was washed by 10 mL of buffer B (50 mM HEPES-KOH, pH 7.6, 500 mM KCl, 5 mM MgCl<sub>2</sub>) and then by 10 mL of buffer A. Then, RNCs were eluted in 3 × 1 mL fractions of buffer A containing 0.1 mg/mL 3 × FLAG Peptide. The total eluate was pooled and was ultra-centrifuged using a TLA55 rotor (Beckman Coulter) at 50,000 rpm at 4°C for 2 h, and the RNC pellet was resuspended into buffer C (50 mM HEPES-KOH, pH 7.6, 100 mM KOAc, 5 mM Mg(OAc)<sub>2</sub>). The final concentration of RNC was 0.5 – 1 μM and stored at –80°C.

The gene coding full-length rabbit SRα and the cytosolic GTPase domain of rabbit SRβ (residues from 60 to 271) was cloned into pET20b and pET24a (Novagen), respectively ([Kobayashi et al., 2018](#)). His-tagged SRα and SRβ were co-expressed in *Escherichia coli* BL21-SI pRARE strain and purified via HisTrap HP column (GE Healthcare) in buffer E (20 mM Tris-HCl, pH 7.6, 150 mM NaCl, 20 mM Imidazole, 5 mM MgCl<sub>2</sub>, 1 mM 2-mercaptoethanol). The sample was then applied to HiTrap SP HP column (GE Healthcare) was eluted by a linear gradient from 150 mM to 1 M. Fractions were concentrated and applied to HiLoad 16/60 Superdex200 (GE Healthcare). Fractions containing SR were pooled, concentrated with Amicon® Ultra-15 (Merck Millipore Ltd) to 37.5 μM, and finally stored at –80°C. Sec61p was purified from solubilized pig pancreatic microsomes in buffer C containing 2% digitonin ([Görlich and Rapoport, 1993](#)). Ribosome-bound Sec61p complexes were first pelleted and Sec61p complexes were released by puromycin and high-salt treatment. Empty ribosomes were pelleted afterward with MLA80 rotor at 60,000 rpm for 2 hours, and the supernatant containing released Sec61p was then applied to HiTrap Q column equilibrated in 50 mM HEPES-KOH, pH 7.6, 10% glycerol, 0.25% digitonin and then eluted over a linear gradient of 1.2 M KOAc. Fractions containing Sec61p were pooled, concentrated and stored at –80°C.

### Purification of recombinant human SRP and SR and GTPase activity assays

Human SRP54, SRP19, SRP9/14, and SRαβΔTM (lacking the nonessential luminal and transmembrane regions of SRβ) were expressed in BL21(DE3)pLysS or Rosetta pLysS cells ([Lee et al., 2018](#)). Human SRP68/72 was co-expressed in yeast strain BCY123 ([Lee et al., 2018](#)). SRP proteins were purified by Ni-NTA affinity chromatography followed by cation exchange chromatography on SP-Sepharose or monoS columns (GE Healthcare). 7SL SRP RNA was *in vitro* transcribed using T7 RNA polymerase and purified on a denaturing polyacrylamide gel. Wild-type and mutant SRPs were assembled by refolding SRP RNA by heating at 95°C for 1 minute and snap cooling on ice for 1 minute, followed by sequential addition of SRP19, SRP68/72, SRP9/14, and SRP54. A typical 600 μL assembly reaction contained 3 μM RNA, 4–6 μM hSRP19, 2.5 μM hSRP68/72, 4 μM hSRP9/14 and 4 μM hSRP54, and was carried out at 37°C for 30 minutes and then at room temperature for 20 minutes. Holo-SRP was purified over a DEAE-Sepharose column as described previously ([Lee et al., 2018](#)).

The reciprocally stimulated GTPase activities of SRP and SR variants were determined as described ([Lee et al., 2018](#)). Briefly, reactions contained 0.2 μM SRP fused to the 4A10L signal sequence, 0.25 μM purified 80S ribosome, indicated concentrations of

SR, and was initiated by addition of 100  $\mu\text{M}$  GTP doped with  $\gamma\text{-}^{32}\text{P}\text{-GTP}$ . Aliquots of the reaction were removed and quenched at specified time points, and were analyzed by thin layer chromatography and autoradiography as described (Peluso et al., 2001). Initial rates were obtained by fits to the linear portion of data. The SRP-independent GTPase reactions of SR were determined in parallel and subtracted to obtain the observed rate constants for the stimulated GTPase reaction between SRP and SR ( $k_{\text{obsd}}$ ). The SR concentration dependencies of  $k_{\text{obsd}}$  were fit to the Michaelis-Menten equation to obtain values of  $k_{\text{cat}}$ .

### Cryo-EM sample preparation

Mammalian SRP (tRNA probes) was mixed with RNCs (final concentration 200 mM) and SR with the final molar ratio 1:1.2:5 in buffer C (50 mM HEPES-KOH, pH 7.6, 100 mM KOAc, 5 mM  $\text{Mg}(\text{OAc})_2$ ) in the presence of either 2 mM GNPPNP or 1 mM GDP, 2 mM Aluminum Fluoride, 8 mM Sodium Fluoride, and 0.25% digitonin. 1  $\mu\text{M}$  of purified Sec61 was added as we observed it improves the distribution of intact RNC·SRP·SR complexes on the grid (Kobayashi et al., 2018). The reaction was incubated at 30°C for 20 minutes after adding SRP, and then another 20 minutes after adding SR. The reaction was finally chilled for 15 minutes on ice. The reaction was applied on Quantifoil R2/2 grids holey carbon grids, which has been coated freshly with an extra layer of carbon and glow discharged with Pelco EasyGlow system for the 15 s. The sample (5  $\mu\text{L}$ ) was incubated on the grid at 4°C with 95% relative humidity for 1–2 minutes before being blotted and then plunged into liquid ethane/propane mix cooled to liquid nitrogen temperature using a ThermoFisher Vitrobot.

Data collection was performed on a Titan Krios electron microscope (ThermoFisher) operated at 300 kV, using the EPU software (ThermoFisher) or SerialEM for automated data acquisition in counting mode using the Gatan K3 direct electron detector and Gatan Imaging Filter with an energy filter slit width of 20 eV. Data were collected at a defocus of  $-1.2$  to  $-2.5$   $\mu\text{m}$  range with step size of 0.1  $\mu\text{m}$  and at a nominal magnification of 81,000x, which resulted into calibrated pixel size of 1.07  $\text{\AA}/\text{pixel}$  (0.535  $\text{\AA}/\text{pixel}$  in super-resolution mode). Illumination conditions were adjusted to an exposure rate of 28  $\text{e}^-/\text{pixel}/\text{second}$ . Micrographs were recorded as movie stacks with an exposure time for each movie stack was 1.4 s, corresponding to an electron dose of  $\sim 50$  electrons/ $\text{\AA}^2$  fractionated into total of 40 frames. Drift and gain reference corrections in addition to dose-weighting were performed with MotionCor2 (Zheng et al., 2017).

### Data processing

Contrast transfer function (CTF) was first calculated using GPU-accelerated computer program for accurate and robust real-time CTF (GCTF) (Zhang, 2016) on electron dose weighted images. The power spectra of the micrographs were then carefully inspected for drift, and only images with signal extending beyond 5  $\text{\AA}$  were retained. A total of 618,786 and 3,848,157 particle-images were picked from the 9,572 and 29,473 dose-weighted frames for the RNC·SRP and the RNC·SRP·SR datasets, respectively, with RELION3 (Zivanov et al., 2018) using a Gaussian blob as a reference. After 25 iterations of two-dimensional (2D) image classification were performed in RELION3 on binned images. Selected particles from 2D classes were refined following the 3D-autorefine approach in RELION3 and using an empty 80S ribosome as a reference filtered to 60  $\text{\AA}$  resolution (See Figures S1 and S3). Images were then subjected to 2 rounds of 3D-focused classification without alignments by applying a circular mask onto the ribosome tunnel exit site. To improve the resolution of the EM density corresponding to the SRP·SR at the SRP RNA distal site, we used the focused refinement approach by subtracting out the signal of the ribosome from the particles before re-centering the picked particle images around SRP·SR density as implemented in RELION3 (Zivanov et al., 2018). Local angular searches were then applied in addition to small angular increments (1.8 degrees), which improved the local resolution of the final reconstruction of the SRP·SR complex from 7  $\text{\AA}$  to 3.6  $\text{\AA}$  (Figure S2). Local resolution and gold standard FSC plots using FSC = 0.143 as a criterion were calculated. Final post-processing of the maps was done in RELION3. Local resolution and gold standard FSC plots using FSC = 0.143 as a criterion were calculated in RELION3. Final maps were sharpened in RELION3.

### Model building

For the model building of the locally refined map of the in the RNC·SRP and SRP·SR complexes obtained from focused 3D refinement, the coordinates of the SRP54, SR, and SRP19, SRP68 RBD, SRP72 RBD, or the 60S subunit (PDB ID: 6FRK, 5M73, 3JAJ) were docked as rigid bodies into the cryo-EM map using USC CHIMERA (Pettersen et al., 2004) and adjusted based on their side chain densities. The C-terminal helices M5 and M6 of the M-domain, the nascent chain and the signal sequence, SRP68 RBD2, the C-terminal helix and tail of SRP72 regions were built *de novo* and their coordinate registry was established based on visible side chains using COOT (Emsley and Cowtan, 2004). For SRP68 RBD2 and the SR $\alpha$  CBR, first a poly-alanine chain was modeled for the visible  $\alpha$  helices and loops. The registry of this region was then established based on the preceding sequence, the density of large and bulky side chains, and the prediction of the location of the  $\alpha$  helices based on homology modeling in PHYRE2 (Kelley et al., 2015) for the first 4 helices. The registry could not be established for the last two C-terminal helices and thus they were left as poly-alanine chain. The EM density of the SRP72 tail was visualized at side chain resolution, which allowed to build the two-turn  $\alpha$  helix insertion and the tail region that followed. The CBR density was assigned based on the preceding sequence of SRX and visible helical turns. Since the M-domain in the late SRP·SR targeting complex was resolved to 4–6  $\text{\AA}$ , the coordinates of the M-domain and signal sequence from the early RNC·SRP targeting complex, where it was resolved at 3.6  $\text{\AA}$ , were used and then docked as rigid bodies into the corresponding density in the late complex. For model refinements, all resulting models were then refined into the corresponding EM densities and subjected to six cycles of real space refinements using phenix.real\_space\_refine in PHENIX (Adams et al., 2010), during

which protein secondary structure, Ramachandran and side-chain rotamer restraints, RNA base-pair restraints were applied. The fit of the EM map was validated using the real space correlation coefficients (CCmask) between the model versus the map Fourier Shell Correlation (FSC) at FSC = 0.5 as a cut-off criterion, which resulted in similar resolution as the half-set map FSC using FSC = 0.143 criterion. Images were prepared in either Chimera ([Pettersen et al., 2004](#)), ChimeraX ([Goddard et al., 2018](#)) or PyMOL.

#### QUANTIFICATION AND STATISTICAL ANALYSIS

The statistical analysis of the cryo-EM data processing, model building and refinements, and the GTPase activity assays, is described in [Method details](#), in [Table 1](#), and in the [supplemental information](#).